Available online at www.sciencedirect.com

ScienceDirect

Advances in Space Research 71 (2023) 4288–4301

ADVANCES IN SPACE RESEARCH (a COSPAR publication)

www.elsevier.com/locate/asr

Application of shaken lattice interferometry based sensors to space navigation

Margaret M. Rybak [a,1,*], Penina Axelrad [a,2], Catie LeDesma [a,3], Dana Z. Anderson [a,4], Todd Ely [b,5]

[a] University of Colorado, Boulder, Colorado 80309, USA
[b] Jet Propulsion Laboratory, Pasadena, California 91109, USA

Received 20 May 2022; received in revised form 9 November 2022; accepted 26 December 2022
Available online 30 December 2022

Abstract

High–sensitivity shaken lattice interferometry (SLI) based sensors have the potential to provide deep space missions with the ability to precisely measure non–gravitational perturbing forces. This work considers the simulation of the OSIRIS-REx mission navigation in the vicinity of Bennu with the addition of measurements from onboard SLI–based accelerometers. The simulation is performed in the Jet Propulsion Laboratory's (JPL) Mission Analysis, Operations and Navigation Toolkit (MONTE) and incorporates OSIRIS-REx reconstructed trajectory and attitude data from the Navigation and Ancillary Information Facility (NAIF) database. The use of the reconstructed data from NAIF provides realistic true dynamical errors and JPL's MONTE software allows for a high–fidelity simulation of an integrated trajectory for the filter. The navigation performance and reduction of tracking and complex modelling enabled by the onboard SLI–based sensor are presented for two orbital phases of the OSIRIS–REx mission. Overall, the results show that the addition of SLI–based accelerometer measurements improves navigation performance, when compared to a radiometric tracking only configuration. In addition, results demonstrate that highly–precise accelerometer measurements can effectively replace at least one day of DSN passes over a three–day period, thereby reducing tracking requirements. Furthermore, it is shown that lower–fidelity surface force modeling and parameter estimation is required when using onboard SLI–based accelerometers.

Keywords: Navigation; Cold; Atom; Interferometry; Accelerometers

1. Introduction

The design of trajectories for successful space exploration missions relies on detailed predictions of the gravitational and non-gravitational forces that will affect the spacecraft motion. During the mission, navigators continue to refine the trajectory predictions based on tracking data. The refinements include improving the fidelity of spacecraft surface models affecting solar radiation pressure and gravity models of target bodies being explored. We are interested in exploring how accelerometers of sufficient sensitivity at low frequencies could enable more precise characterization of non–gravitational forces acting on the

* Corresponding author.
E-mail addresses: margaret.rybak@colorado.edu (M.M. Rybak), penina.axelrad@colorado.edu (P. Axelrad), catherine.ledesma@colorado.edu (C. LeDesma), dana@jila.colorado.edu (D.Z. Anderson), todd.a.ely@jpl.nasa.gov (T. Ely).
[1] Graduate Student, Smead Aerospace Engineering Sciences, University of Colorado, Boulder.
[2] Smead Aerospace Engineering Sciences, Fellow AIAA, University of Colorado, Boulder.
[3] Graduate Student, JILA Physics, University of Colorado, Boulder.
[4] JILA Physics Fellow, University of Colorado, Boulder.
[5] Principal Investigator, Deep Space Atomic Clock, Jet Propulsion Laboratory, California Institute of Technology.

https://doi.org/10.1016/j.asr.2022.12.050
0273-1177/

spacecraft. This configuration could alleviate the modeling and tracking requirements for a mission, as well as provide better navigation performance. Advances in cold atom interferometry (CAI) have demonstrated the potential to provide highly sensitive measurements of acceleration with small biases, and negligible scale factor and drift (Jekeli, 2006; Battelier, et al., 2016; Reguzzoni, Migliaccio, & Batsukh, 2021). Shaken Lattice Interferometry (SLI) has further adapted CAI technology by trapping the atoms in the nodes of an electromagnetic standing wave. This configuration allows for longer interferometric sequence times and thus higher sensitivity than free–space propagation CAI–based sensors. The interferometric sequence time for SLI–based sensors is not tied to the size of the device, as in the case of conventional CAI–based sensors, thereby supporting their potential miniaturization to dimensions suitable for use onboard spacecraft (Weidner, 2019; Theurkauf, 2020). This research explores how onboard measurements from SLI–based accelerometers could be leveraged in a deep space mission to reduce the modeling and tracking burden.

Ultra–sensitive electrostatic accelerometers (EAs) were used on both the Gravity Recovery and Climate Experiment (GRACE) and Gravity field and steady-state Ocean Circulation Explorer (GOCE) missions. The goal of these missions was to precisely map the Earth's gravity field using highly–sensitive onboard EAs to measure the gravity gradient and non–gravitational accelerations. The sensitive EAs were critical to the success of GRACE and GOCE, however they required frequent calibration due to their long term noise instability (Visser, 2008; Rummel, Yi, & Stummer, 2011; Christophe B., 2013; Klinger & Mayer-Gurr, 2016; Peidou & Pagiatakis, 2019; Fan, Liang, Wang, & Luo, 2022). CAI–based accelerometers have been proposed for use on future gravity mapping missions due to their noise stability at low frequencies compared to the performance of EAs (Carraz, Siemes, Massotti, Haagmans, & Silvestrin, 2014; Chiow, Williams, & Yu, 2015; Hogan & Kasevich, 2016; Migliaccio, et al., 2019; Leveque, et al., 2021). Research has also considered the concept of hybridizing electrostatic and CAI–based accelerometers to capture the different sensor performance advantages (Jekeli, 2005; Christophe, et al., 2017).

Conventional and CAI–based accelerometers have also been considered for use in navigation applications. Prior work by Bhatia and Geller (2020) investigated the use of pairs of CAI–based accelerometers as ultra–precise inertial gradiometers for autonomous navigation. They evaluated the navigation performance of using measurements from onboard CAI–based accelerometers correlated to onboard gravity maps to determine orbital information. Canciani (2012) performed a simulation analysis of an aircraft using a combination of an aviation grade inertial navigation system and CAI–based accelerometer measurements to improve performance. Jekeli (2005) presented an analysis of the integration of CAI–based sensors into a free–inertial navigation system and implications for navigation error improvement. Both Canciani and Jekeli focused on the method of dead–reckoning, which uses accelerometer measurements to directly propagate the position and velocity states of a vehicle. Alternately, Ely, Heyne, and Riedel (2012) investigated a method for using measurements from a conventional accelerometer directly in a navigation filter for the Altair lunar lander.

Our work focuses on how onboard SLI-based accelerometers could be leveraged to precisely measure the non–gravitational forces during a deep space mission. The method follows the approach used by Ely, Heyne, and Riedel where measurements from the accelerometer are used directly in the navigation filter. The Origins, Spectral Interpretation, Resource Identification, Security-Regolith Explorer (OSIRIS-REx/OREx) mission to the asteroid Bennu was selected as a case study for this research. Actual OREx mission data from the Navigation and Ancillary Information Facility (NAIF) is used to provide the most realistic dynamic error profiles possible. The acceleration magnitudes and profiles experienced onboard OREx are investigated to identify the performance metrics required for a viable SLI–based accelerometer. Simulated SLI–based accelerometer measurements are then integrated into a high–fidelity simulation, in the Jet Propulsion Laboratory's (JPL) Mission Analysis, Operations and Navigation Toolkit (MONTE), of the OREx navigation for two orbital phases. During the OREx mission, optical–navigation and landmark tracking were used in addition to DSN tracking. To understand the impact specific to using onboard accelerometers, this study considers estimation using only DSN tracking and SLI–based accelerometer measurements. The navigation results for DSN alone and DSN with accelerometer measurements are compared, to assess the effectiveness of the onboard accelerometers in reducing the orbit estimation errors and the requirements for both DSN tracking and dynamic modeling.

The rest of this paper is organized as follows. Section 2 provides the background and current performance of CAI/SLI–based sensors and their advantages over current state–of–the–art EA technology. Section 3 describes the motivation for the selection of the OREx mission as a case study and details the dynamic models used to simulate the OREx orbit. Section 4 presents the methods for simulation of DSN and SLI–based accelerometer measurements and the navigation filter set–up. Section 5 provides an analysis of the navigation performance for the OREx mission simulation, using measurements from the DSN in addition to the onboard SLI–based measurements. The paper concludes in Section 6 with a summary of findings and suggestions for future work.

2. Cold atom interferometry based accelerometers

Conventional accelerometers, such as mechanical or electrostatic sensors, measure the restoring force required to hold a proof mass steady in a null position within the housing or platform on which the unit is mounted. The

restoring force is sensed to determine the acceleration on the proof mass and thereby the nongravitational forces acting on the platform (Conklin, 2015). Electrostatic accelerometers (EA) have been used onboard spacecraft since the late 1970′s. The CASTOR D5B mission used the CACTUS accelerometer to measure the surface forces on the satellite. (Touboul, Foulon, Rodrigues, & Marque, 2004). EAs were used on both the Gravity Recovery and Climate Experiment (GRACE) and Gravity field and steady-state Ocean Circulation Explorer (GOCE) missions. For the GRACE mission the EAs were used to sense non–gravitational forces, including drag, solar radiation pressure, Earth albedo, thruster firings and magnetic torque accelerations on the spacecraft. Accurate measurement of the non–gravitational forces combined with precise radiometric measurements enabled high-fidelity mapping of the Earth's gravity field. Onboard GOCE, three pairs of EAs were used as a gradiometer to measure the gravity gradient along the orbit (Touboul, Willemenot, Foulon, & Josselin, 1999; Flury, Bettadpur, & Tapley, 2008). The EAs onboard the GRACE and GOCE missions achieved accuracies of 10^{-10} m/s^2/$\sqrt{}$Hz and 10^{-12} m/s^2/$\sqrt{}$Hz (normalized for a 1–s integration period) respectively (Touboul P., 2003; Flury, Bettadpur, & Tapley, 2008). However, these sensitivities were restricted to specific measurement bandwidths of 2x10^{-4} to 0.1 Hz for GRACE (Kang, Tapely, Bettadpur, Ries, & Nagel, 2006) and 5x10^{-3} to 0.1 Hz for GOCE (Touboul, Willemenot, Foulon, & Josselin, 1999). At lower frequencies, beyond these measurement bands, the noise increases with 1/f and with bias instability noise, typical for conventional accelerometers (Christophe, Marque, & Foulon, 2010; Christophe B., 2013; Christophe, et al., 2017; Fan, Liang, Wang, & Luo, 2022). While this performance limitation was not detrimental for their mission objectives, it does mean that the measurements could not be used directly to support navigation (Rummel, Yi, & Stummer, 2011).

CAI–based accelerometers were first developed in the early 1990′s and have been shown to provide sensitivities that far exceed the performance of conventional mechanical and electrostatic sensors (Clauser, 1988; Kasevich & Chu, 1991; Carnal & Mlynek, 1991). The interferometry sequence is performed by loading an atom cloud into a magneto-optic trap where the atoms are cooled to micro-Kelvin level to reduce their velocities. The atom cloud is then excited by laser pulses, separating it into counter-propagating clouds along the axis of acceleration. The atoms are equally divided into states of opposite momentum, analogous to the splitting of photons at the half-silvered mirror in a traditional Michelson interferometer. The incident acceleration on the sensor causes a phase difference to accumulate between the two propagating clouds over the interrogation time. A final laser pulse recombines the clouds, generating an interference pattern representative of the difference in propagation paths. The acceleration can then be deduced from the interference pattern (Kasevich & Chu, 1991). The potential advantage of using CAI–based accelerometers is that, unlike EAs, the underlying physics does not introduce any systematic errors or drift, dramatically reducing the requirements for calibration. CAI–based sensors display white noise at all frequencies below at least 100 mHz (Canuel, et al., 2006; Meunier, et al., 2014; Dutta, et al., 2016). This facilitates their use in making absolute acceleration measurements which can be used directly for navigation (Canuel, et al., 2006; Christophe, et al., 2017; Abrykosov, et al., 2019; Trimeche, et al., 2019).

Longer interrogation times improve the phase difference resolution for CAI, thereby providing greater sensor sensitivity. On Earth, interrogation times of conventional CAI–based sensors are limited by the atom free-fall time due to gravity. Ground based CAI–based accelerometer studies have shown potential acceleration sensitivities of 1x10^{-8} m/s^2/$\sqrt{}$Hz (Jekeli, 2005; Kasevich, 2007). However, in zero–g, much longer interrogation times can be achieved. Nyman et al. (2006) presented a potential sensitivity of 1.8x10^{-10} m/s^2/$\sqrt{}$Hz for a CAI–based accelerometer tested in zero–g, detailed in Table 1. The amplitude spectral power density is scaled for the 15-s interferometric sequence time, as shown in Eq. (1).

$$\sigma(15s) = \frac{1.8\text{x}10^{-10}\frac{m}{s^2}}{\sqrt{Hz}\sqrt{15s}} = 4.7\text{x}10^{-11}\frac{m}{s^2} \quad (1)$$

Unlike the continuous measurement capability of conventional accelerometers, CAI–based accelerometers can only measure acceleration during the interrogation time of each duty cycle. There are dead bands between measurements, during which the atom cloud is cooled and prepared for the next interferometry sequence (total time minus interrogation time, 5 s in the case in Table 1). Hybrid accelerometer configurations have been proposed to take advantage of the high-rates and high-precision of EAs at higher frequencies, and the stability of the CAI at lower frequencies (Lautier, et al., 2014; Christophe, et al., 2017; Abrykosov, et al., 2019). Following the work presented in Jekeli (2005), measurements from the combination of multiple accelerometers can be treated as a single measurement with combined accelerometer noise properties. Meunier et al. (2014) proposed an alternative approach of joint interrogation of up to five different atom clouds to remove dead time; which also resulted in improved sensitivity of 1x10^{-13} m/s^2 at a 60 s interrogation time. For the purposes of this work, it is assumed that either multiple CAI–based accelerometers are used with staggered sequence start times

Table 1
Nyman Accelerometer Best Case Performance Metrics (Nyman, et al., 2006).

Amplitude Spectral Density	1.8x10^{-10} m/s^2 /$\sqrt{}$Hz
Sensitivity per Shot	4.7x10^{-11} m/s^2 /shot
Interferometric Sequence Time	15 s
Interrogation Time	10 s

to cover dead bands, or the multi–cloud approach is used, thereby providing continuous measurement capability. At this time, additional technical advancements are still required to reduce the size, weight, and power of future multi-axis CAI-based systems that could support this type of space deployment.

In most CAI-based sensors the cloud of cold atoms is released, and the necessary interferometer steps are performed during its free-fall. With this method, interrogation time is tied to the free-fall distance, and therefore the sensitivity is constrained by the size of the apparatus. The sensitivity can be decoupled from cavity size by instead, confining the atoms to an optical lattice, where splitting/recombination and propagation are carried out by modulating the phase of the lattice. Machine learning techniques are used to determine effective shaking functions to achieve the desired sensor response to input accelerations (Weidner, Yu, Kosloff, & Anderson, 2017; Weidner & Anderson, 2018; Weidner & Anderson, 2018; Weidner, 2019; Theurkauf, 2020). Using shaken lattice interferometry (SLI), improved sensitivities can be achieved by increasing the interrogation time, which is made possible by suspending the atoms in the lattice. Interrogation times of up to 20-s, a duration completely infeasible in 1-g for conventional CAI, have been realized experimentally (Xu, et al., 2019).

By confining atoms to a 3D lattice and loading atoms that have condensed into a Bose-Einstein Condensate (BEC), high atom numbers with narrow velocity distributions can also yield increased sensitivities. Atom-atom interactions, which occur when atoms become denser with decreasing temperature, can cause phase errors due to their effect on both atom coherence and heating. By implementing a 3D lattice, interactions can be lowered by sparse population of the lattice through the use of a deep two-dimensional lattice with low single-site occupation. This results in an array of 1-D low atom number interferometers with shaking then taking place along the third dimension. This approach allows total atom numbers to reach 10^6, lowering shot noise to levels comparable with state-of-the art atom interferometers.

A high repetition rate of the interferometric sequence is also feasible for SLI if an all-optical approach is taken for the generation of BEC. This involves using high powered laser beams instead of magnetic fields to perform evaporative cooling where atoms are cooled to degeneracy and form a BEC. By dynamically controlling these optical traps, experimental repetition times under 2-s have been achieved (Albers, 2020) and those under 1-s proposed (Roy, Green, Bowler, & Gupta, 2016). SLI therefore has the potential to enable sensors with high sensitivities that are much smaller than existing CAI–based devices, and thus more suitable for use on spacecraft. There is still much work to be done on developing compatible low size, weight, and power laser systems that can effect the necessary lattice control.

3. OREx case study

The science orbits of the OSIRIS-REx spacecraft in close proximity to the asteroid Bennu were selected as a case study for this research because they capture the quite interesting and unique navigation challenges faced when exploring a distant, small-body asteroid. In the very low gravity environment of Bennu, the non–gravitational perturbing forces, such as solar radiation pressure (SRP) and spacecraft thermal radiation have a larger influence on the spacecraft motion compared with orbits around Earth or other planets. The large distance from Earth reduces the observability of an orbit based only on radiometric tracking from the Earth, and, in this exploration phase, the full gravitational field of the small body has not yet been established. The success of the OREx mission was achieved with a combination of extensive Deep Space Network (DSN) tracking, altimetry measurements, optical navigation, and the development of high-fidelity non–gravitational force models (Hesar, Scheeres, & McMahon, 2016; Williams, et al., 2018). The dominant non–gravitational perturbing force on the OREx trajectory was SRP, and basic modeling proved to be insufficient in representing its full effect on the spacecraft. In particular, Geeraert et al. (2020) described how in certain orbit configurations, the errors in the SRP model were aliasing into the gravity field estimation. To reduce the navigation errors due to SRP and improve the gravity recovery, the navigation team created a compleX ray-trace SRP model. This model included self–shadowing and effects due to ray bounces between the spacecraft surfaces. In addition, complex models for the spacecraft thermal radiation, Bennu Albedo (ALB) and high gain antenna (HGA) transmission pressure were developed and used (Berry, et al., 2015; Geeraert, et al., 2020). A successful touch–and–go maneuver, to collect a sample from Bennu's surface, required predicted state error resolution of tens of meters, and perturbing acceleration characterization at the level of 3 nm/s^2 (Antreasian, et al., 2016). This requirement was ultimately met with the implementation of complex models, daily 5 to 8-hrs DSN radiometric tracking, Bennu landmark tracking, and altimetry measurements (Getzandanner, et al., 2016).

3.1. Simulation overview

To study the potential benefits of onboard SLI–based accelerometers for orbit determination in the vicinity of a small body, like Bennu, we have developed a simulation based on the OREx mission. A traditional orbit determination approach is assumed where observations of the true spacecraft trajectory and a predicted or reference trajectory are processed in a Kalman Filter to produce an estimate of the spacecraft's true trajectory. The simulation is constructed using the Jet Propulsion Laboratory's (JPL) Mission Analysis, Operations, and Navigation Toolkit (MONTE) software. MONTE allows orbit propagation

and estimation modeling for virtually any mission scenario (NASA: Jet Propulsion Laboratory, 2021). Our MONTE simulation directly imports an OREx "truth" trajectory and spacecraft attitude based on actual mission data obtained from the Navigation and Ancillary Information Facility (NAIF) database. This best-estimate NAIF trajectory was constructed by the OREx team from data received throughout the mission. Using this trajectory as a truth reference gives our simulation a high degree of realism and fidelity.

The reference trajectory for the Kalman Filter is generated using MONTE's astrodynamic model libraries, populated with relevant spacecraft and relevant celestial body parameters produced by the navigation team to support the mission. To validate which models are used and how they are configured the MONTE models are evaluated along the true NAIF trajectory. This evaluation includes the exact parameters, such as for the gravity model and thermal data, that were used for the NAIF reconstruction. The resulting MONTE propagated trajectory is then compared to the NAIF trajectory to show they only differ due to the fidelity of the non–gravitational force models implemented for the NAIF–truth reconstruction by the OREx team versus the propagation in MONTE. The filter reference trajectory is then generated using the validated MONTE models with fidelity based on the knowledge or parameter values used during the specific mission phase. In addition, the filter reference trajectory is modified to include initial condition and gravity errors for the Monte Carlo analysis.

The rest of this section is organized as follows. The trajectory and attitude data from NAIF, used as the truth for this simulation, are presented. The models used and the setup parameters for the filter reference trajectory generation in MONTE are then detailed. Finally, the trajectory estimation process is validated via comparison with the NAIF–truth trajectory.

3.2. NAIF-truth trajectory

Two timeframes were selected for simulation, shown in Table 2, which occur during the Orbit A and B phases of the OREx mission. The Orbit A phase began on December 31, 2018, with a nominal orbit radius of 1.5 km. Orbit A was used to establish Bennu landmark tracking and characterize orbit navigation and maneuver performance. Orbit B began on June 12, 2019, with a nominal radius of 1 km. Orbit B was used primarily for radio science, establishing an accurate Bennu shape model, and determining a feasible landing site for sample collection (Lauretta, et al., 2017).

These two phases were chosen to provide orbits with different radii and Sun-Bennu distances, resulting in distinct gravity and non–gravitational force profiles and magnitudes. From Orbit A to Orbit B the reduction in altitude results in an order of magnitude increase in perturbing accelerations from gravity; while a larger Sun–Bennu distance reduces the SRP and spacecraft thermal radiation magnitudes, shown later in Fig. 3. Fig. 1 shows the two orbit orientations, indicating the radial (green), transverse (blue), and orbit normal (red) (RTN) directions at the start of each phase. Each orbit is shown from the perspective of Earth, looking directly towards Bennu. Both orbits lie in the terminator plane, with the normal direction aligned with the Sun–vector. The OREx team chose this orientation to remove the complication of OREx passing into Bennu's shadow, thereby providing better stability with respect to SRP and temperature effects (Lauretta, et al., 2017).

Table 2
Simulation Timeframes.

Orbit A	Orbit B
February 8 – 12, 2019	July 12 – 16, 2019

The spacecraft frame is shown in Fig. 2. The + X axis is oriented through the face containing the HGA. The + Z axis is oriented along the face containing the low–gain antenna and the + Y axis completes the right-handed frame (Semenov, 2014; Lauretta, et al., 2017). During Orbits A and B, OREx was primarily oriented with Z–axis aligned in the nadir–direction and the + X–axis, aligned with the Sun–vector (hence predominantly in the orbit normal direction). Once a day the spacecraft is slewed to point the HGA antenna towards Earth for DSN radiometric tracking for up to 5-hrs per day (Williams, et al., 2018).

For the purposes of this work, the state vectors are propagated and estimated in the filter in the Earth's Mean Equator and Mean Equinox or EME2000 frame. The non–gravitational acceleration profiles are presented in the spacecraft XYZ frame due to their strong correlation with the spacecraft pointing directions. The filter results are mapped to the RTN frame to allow for comparison with mission analysis presented by the OREx navigation team.

3.3. MONTE simulated filter reference trajectory

The integrated trajectory for the filter is simulated using both point mass (Gm) and higher–order gravity, SRP, and Albedo (ALB) acceleration models, populated with OREx and Bennu parameters. A time history of the acceleration due to spacecraft thermal radiation pressure, provided by the NASA/KinetX team, is included in the model validation (J. Leonard and J. Geeraert personal communication, Sept 3, 2021). The set–up for each acceleration model is validated and then used to generate the integrated trajectory, populated with the model fidelity available during the mission phase.

3.3.1. Acceleration modeling for OREx

The OREx spacecraft is modelled using nine flat plates to represent the -X and +/–YZ bus faces and the front and back of each solar array; and a parabolic dish for the HGA. The specular and diffuse coefficients, shown in Table 3, are based on Germanium Kapton multilayer insulation for the bus and HGA, and general material properties for solar panels, as presented in Kenneally (2019).

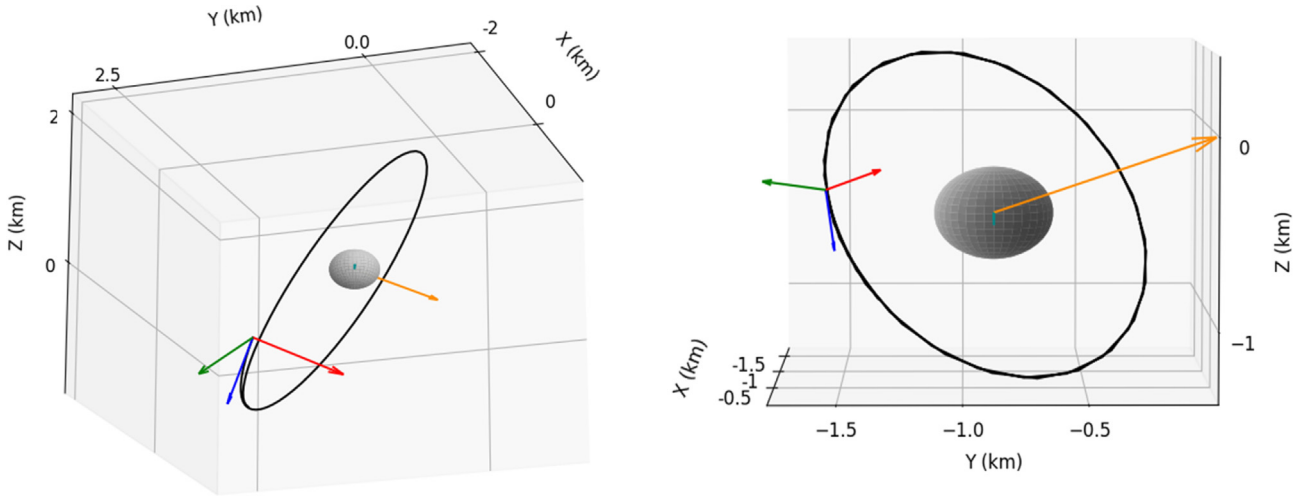

Fig. 1. OREx Orbit A (left) and B (right) orbit orientations. Unit vector to Sun shown in gold and viewpoint oriented along unit vector to Earth, shown in cyan. Size of orbit and average asteroid radius shown to scale.

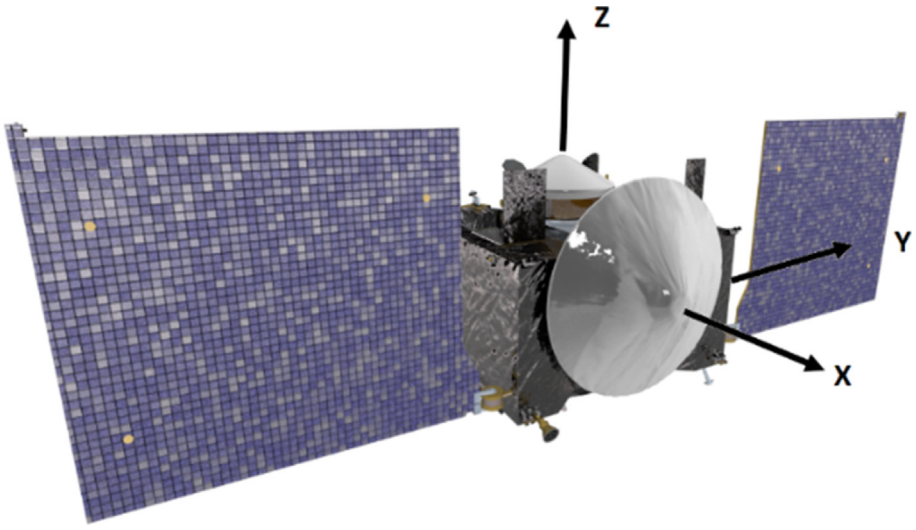

Fig. 2. OREx (OSIRIS-REx Asteroid Sample Return Mission, 2022) with spacecraft coordinate axes added (Lauretta, et al., 2017).

The spacecraft bus attitude is provided from the NAIF database. The solar array baseplate frames, fixed to the bus attitude, are then obtained via a 180° rotation about the Z axis and –90° degree rotation about the X axis for the + Y array, and a 90° rotation about X for the -Y array. The rotations of the gimbal frames from NAIF, defined about the baseplate frames, are then used to define the attitude profiles for each solar array (Semenov, 2014).

The filter trajectory SRP and ALB profile generation uses the spacecraft shape model and orientation data to determine the force incident on each spacecraft component. The effect on each component is then combined into an overall acceleration. Bennu is modeled as a simple sphere with a diameter of 490–km (Barnouin, et al., 2019) with thermophysical coefficients used in the ALB simulation shown in Table 4.

Both models use the orientation of the spacecraft components to determine effective area, but do not account for self-shadowing i.e., if one surface is blocking another from the incident rays. Bennu's gravity model is simulated with the Gm gravitational parameter and the 16x16 sized spherical harmonic (SPH) field representation used during the actual NAIF trajectory reconstruction, provided by the NASA/KinetX team (J. Leonard and J. Geeraert personal communication, Sept 3, 2021).

3.3.2. MONTE model comparison to NAIF trajectory

To validate each acceleration component set-up in MONTE, the component of interest is evaluated along the NAIF–truth trajectory, populated with the OREx and Bennu parameter values used at the time of NAIF trajectory reconstruction. The profile is then compared to the full NAIF–truth acceleration minus the profiles of all but the acceleration of interest, each evaluated along the NAIF–truth. This comparison confirms that the correct set–up parameters have been chosen. The full 16x16 SPH

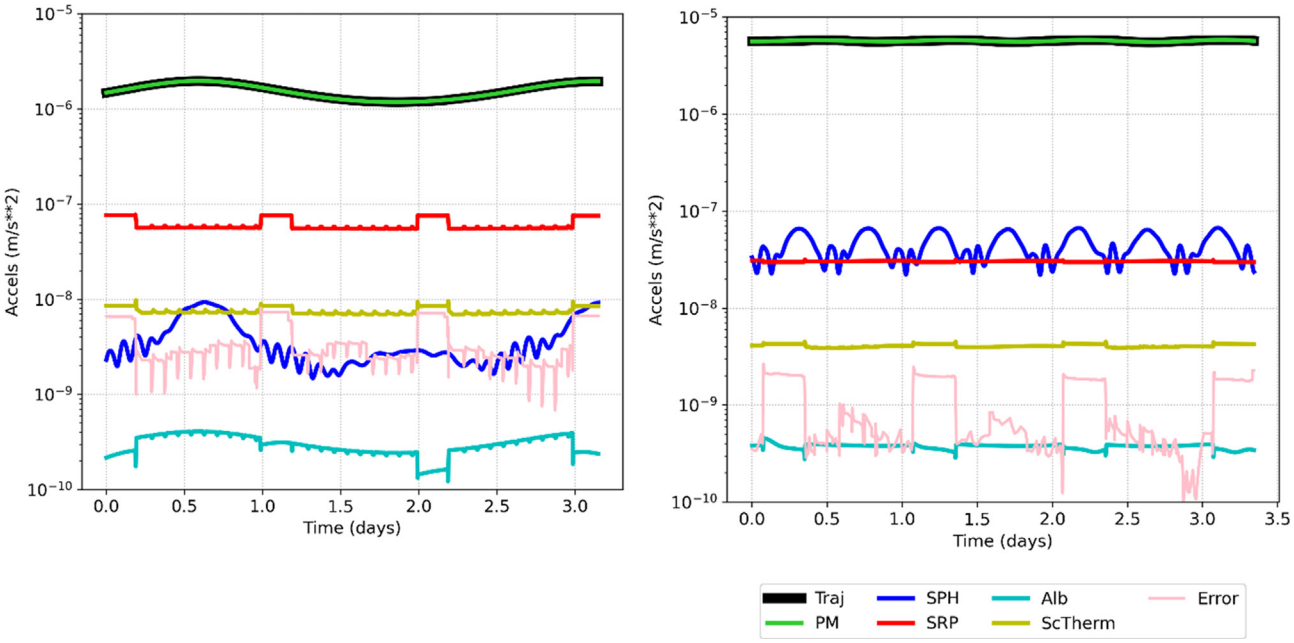

Fig. 3. Simulated Acceleration Magnitudes of OREx in Orbit A (left) and B (right).

Table 3
Spacecraft SRP Model Parameters (Kenneally, 2019).

Component	NAIF Frame ID	Normal Vector	Spec Ref Coef.	Diff Coeff.	Shape	Area (m^2)
+X bus	−64000	[1, 0, 0]	0.408	0.102	Parabolic Dish	2.1 m diameter, 0.4 m depth
-X bus		[-1, 0, 0]			Flat Plate	4.8
+/- Y bus		[0, +/-1, 0]				5.76
+/- Z bus		[0, 0, +/-1]				
+/- Y Front Solar Panel	−64012	[0, 0, 1]	0.088	0.022		4.25
+/- Y Back Solar Panel	−64022	[0, 0, −1]	0.00	0.05		

Table 4
Bennu Thermophysical Properties (Rozitis, et al., 2020).

Component	Coefficient
Albedo	0.02
Thermal Emissivity	0.95

field, Gm, and the thermal radiation acceleration profile are used for the validation process. Fig. 3 shows the resulting acceleration profiles obtained for the total acceleration (black), Gm (green), SPH (blue), SRP (red), ALB (cyan), and spacecraft thermal radiation (gold) accelerations, evaluated along the NAIF–true trajectory. The acceleration profiles and magnitudes are consistent with those generated by the OREx team for both orbit phases, as presented in Antreasian, et al. (2016) and Leonard, et al. (2019). To determine the difference between the total NAIF reconstructed and combined acceleration models, the Gm, SPH, SRP, ALB, and thermal acceleration models (ScTherm), evaluated along the true NAIF trajectory, are subtracted from the total NAIF trajectory acceleration profile, shown in pink on Fig. 3.

Fig. 4 shows a comparison between the NAIF–true trajectory acceleration minus the Gm and SPH models evaluated along the NAIF–true trajectory and the SRP, ALB and thermal radiation models evaluated along the NAIF–true trajectory. This shows the difference between the NAIF–true non–gravitational acceleration, used as the truth for this study, and non–gravitational acceleration models set–up in MONTE. This is the pink profile from Fig. 3, shown in terms of its XYZ components in the spacecraft frame in Fig. 4.

Fig. 5 shows the differences between the two acceleration profiles presented in Fig. 4. The difference between the true and modelled accelerations evaluated along the true trajectory, is primarily due to the 9 plates plus cone HGA SRP model used. This SRP model uses imperfect spectral and diffusion coefficients, an overly simplistic HGA model, and does not account for self-shadowing or solar ray bounces between surfaces. The mismodeling is made more apparent by once per day attitude maneuvers to orient the high gain antenna (HGA) toward the Earth. The change of Sun exposure on the different spacecraft surfaces in the Earth pointing, versus the nominal Sun pointing orientations, results in significant jumps in the SRP profile, that can be seen at the start of each day in Fig. 5. Additional spikes are also present in the Orbit A total

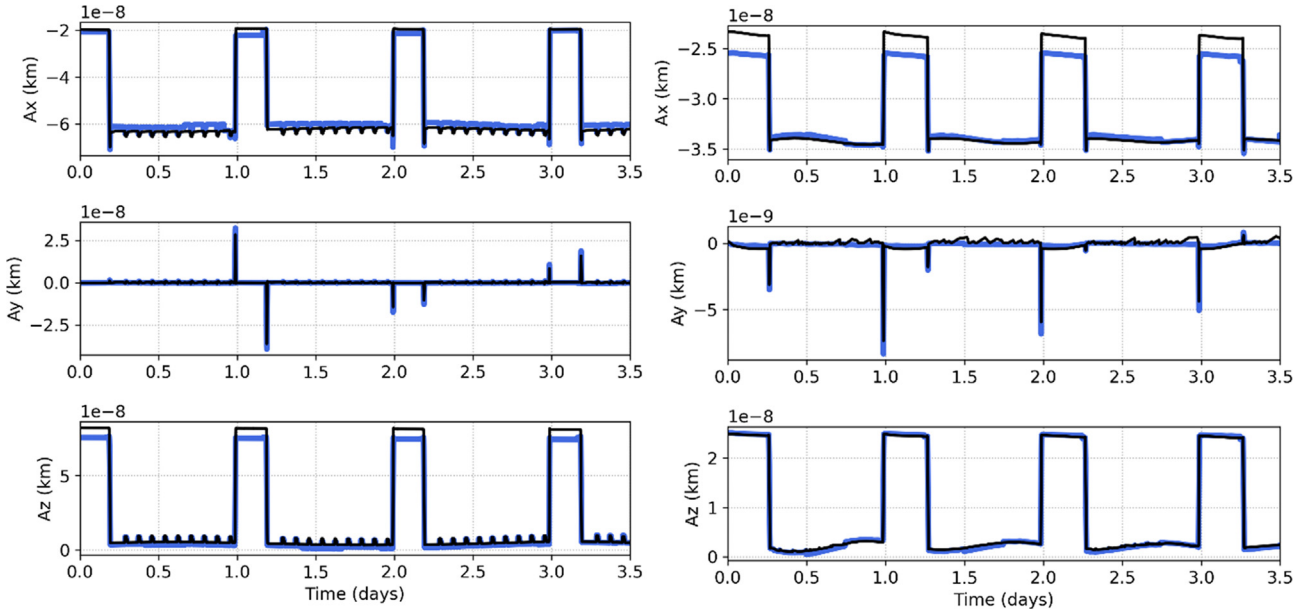

Fig. 4. Comparison of the NAIF–true non–gravitational profile (blue) and the non–gravitational acceleration models (SRP, ALB, and thermal radiation) evaluated along the NAIF–true trajectory (black) for Orbit A (left) and Orbit B (right) expressed in the spacecraft frame.

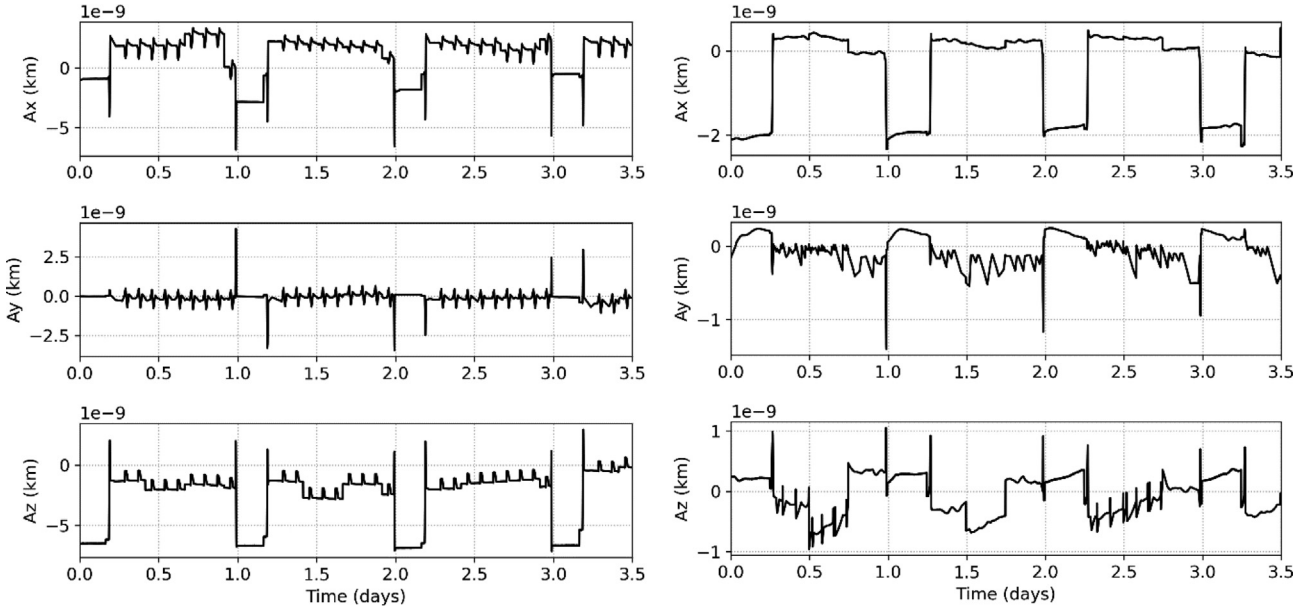

Fig. 5. Difference between the NAIF–true non–gravitational profile and the non–gravitational acceleration models (SRP, ALB, and thermal radiation) evaluated along the NAIF–true trajectory for Orbit A (left) and Orbit B (right) expressed in the spacecraft frame.

and differenced profiles when OREx performs imaging sweeps of Bennu for optical navigation, seen between the larger daily HGA–pointing maneuvers (Williams, et al., 2018).

The differences introduced by the SRP mismodeling are consistent with those documented by the OREx team for Orbit A when using a simplified SRP model (Geeraert, et al., 2020). The team saw differences on the order of $1x10^{-9}$ m/s^2 in X and $6x10^{-9}$ m/s^2 in Z in the Earth pointing orientation. To reduce these effects, they developed and incorporated complex HGA and ray-trace SRP models into the OREx mission navigation process (Leonard, et al., 2019). For our study, onboard SLI–based accelerometers will measure the total non–gravitational accelerations, including the signature that is mismodeled in the filter propagation, seen in Fig. 5. This will allow an analysis of how well the mismodeled accelerations can be compensated for in the filter using the accelerometer measurements. If

the mismodeling can be sufficiently captured by the accelerometer measurements, then modeling requirements, such as the need for the complex SRP model, could potentially be reduced.

4. OREx measurement simulation and navigation filter setup

The position and velocity of OREx are estimated in a conventional Kalman filter. DSN radiometric tracking measurements and SLI–based accelerometer measurements are simulated along the true trajectory, including relevant sensitivity levels. The filter propagates the reference trajectory and processes the DSN radiometric and accelerometer measurements. The initial condition error for Orbit A is 1 m position and 0.1 mm/s velocity 1σ. This error is based on an approximation of the trajectory error predicted by the OREx team at data cutoff in Reference (Geeraert, et al., 2020), when using an optimized antenna + 9–plate SRP model. For Orbit B, initial condition errors of 0.3 m and 0.03 mm/s 1σ are used, based on the state errors predicted by the OREx team at data cutoff in Reference (Williams, et al., 2018). The reference trajectory includes Gm and 3x3 SPH gravity, with 1σ gravitational parameter error (Gm) of 2.44x10^{-12} km^3/s^2 (0.15 % of Gm) (Williams, et al., 2018) (Antreasian, et al., 2016; Williams, et al., 2018; Leonard, et al., 2019; French, 2020). The simple 9–plate + HGA spacecraft model is used in the SRP and ALB models. During navigation analysis of the OREx mission, presented in Leonard, et al. (2019) and Berry, et al. (2015), a 3σ SRP scale factor error of 10 % was used. For the purposes of this simulation, SRP errors are present due to the simplified SRP model, so no additional scale factor error is applied. Acceleration due to the spacecraft thermal radiation pressure is not included in the filter model evaluation.

4.1. Simulated DSN measurements

During both Orbit A and B phases of OREx radiometric tracking from the DSN was available for approximately 5-hrs per day on the HGA with up to an additional 3-hrs on the low–gain antenna. For the actual OREx mission, the two–way range noise was 3 m 1σ to account for hardware biases, ionosphere, and solar plasma effects. The X-band (~8.45 GHz) Doppler noise for a 60 s count time was 0.1 mm/s 1σ, for 2–way (Williams, et al., 2018). In our simulation, two-way range and Doppler measurements are created at a 60 s time step, including the 3 m and 0.1 mm/s noise error respectively. The simulated measurement passes are aligned with the HGA Earth–pointing attitude times, i.e., the times when the daily large steps occur in the profiles shown in Fig. 4, using the DSN station in view during that interval. These passes occur daily and are approximately 5-hrs long.

4.2. Simulated accelerometer measurements

Accelerometers sense the non-gravitational forces incident on a spacecraft (Titterton & Weston, 2004; Jekeli, 2005; Jekeli, 2006). To simulate accelerometer measurements of the OREx true trajectory, the validated Gm and 16x16 SPH gravity model is evaluated along the trajectory. This gravitational acceleration ($\vec{a}_{true,\,Grav}$) is then subtracted from the total acceleration profile ($\vec{a}_{true,\,Total}$), leaving the non–gravitational acceleration ($\vec{a}_{NG}$), as shown in Eq. (2).

$$\vec{a}_{NG} = \vec{a}_{true,\,Total} - \vec{a}_{true,\,Grav} \tag{2}$$

Following the work of Ely, Heyne, and Riedel (2012), the accelerometer measurements are simulated as delta–velocity measurements of Euler integrated accelerations over the measurement sample period, i.e. the interferometric sequence time, shown in Eq. (3),

$$\Delta V(t_n) = \sum_{i=1}^{n-1}[I + \Sigma + \Lambda + \Omega][a_{ng}(t_i) + b + v(t_i)][t_{i+1} - t_i] \tag{3}$$

where measurements are taken every 60-s and n is the sample counter, v is the Gaussian white noise accelerometer error, Σ is the scale factor error, Λ is the misalignment error, Ω is the orthogonality error, and b is the bias error. Internally, the accelerometer is accumulating the acceleration over 60-s.

Based on the range of potential performance metrics for SLI–based accelerometers, multiple accelerometer sensitivities are investigated, shown in Table 5. The sensitivities are presented as amplitude spectral density power and per shot following the calculation shown in Eq. (1).

Fig. 6 shows the simulated accelerometer measurements, observed along the true trajectory, and the measurements computed by the filter along the reference trajectory. The computed measurements, computed along the reference trajectory, include a realization of the injected error sources and initial condition error. The observed measurements shown are generated for the 1x10^{-9} m/s^2 accelerometer sensitivity.

The discrepancy between the simulated observed and computed measurements is due to the simplified models used in the filter propagation and the initial condition errors applied. The most significant effect is from the simplified model of the HGA on the + X spacecraft face,

Table 5
Investigated Accelerometer Sensitivities.

Sensitivity per Shot	1x10^{-8} m/s^2 /shot	1x10^{-9} m/s^2 /shot	1x10^{-10} m/s^2 /shot
Amplitude Spectral Density	7.75x10^{-8} m/s^2 /$\sqrt{}$Hz	7.75x10^{-9} m/s^2 /$\sqrt{}$Hz	7.75x10^{-10} m/s^2 /$\sqrt{}$Hz

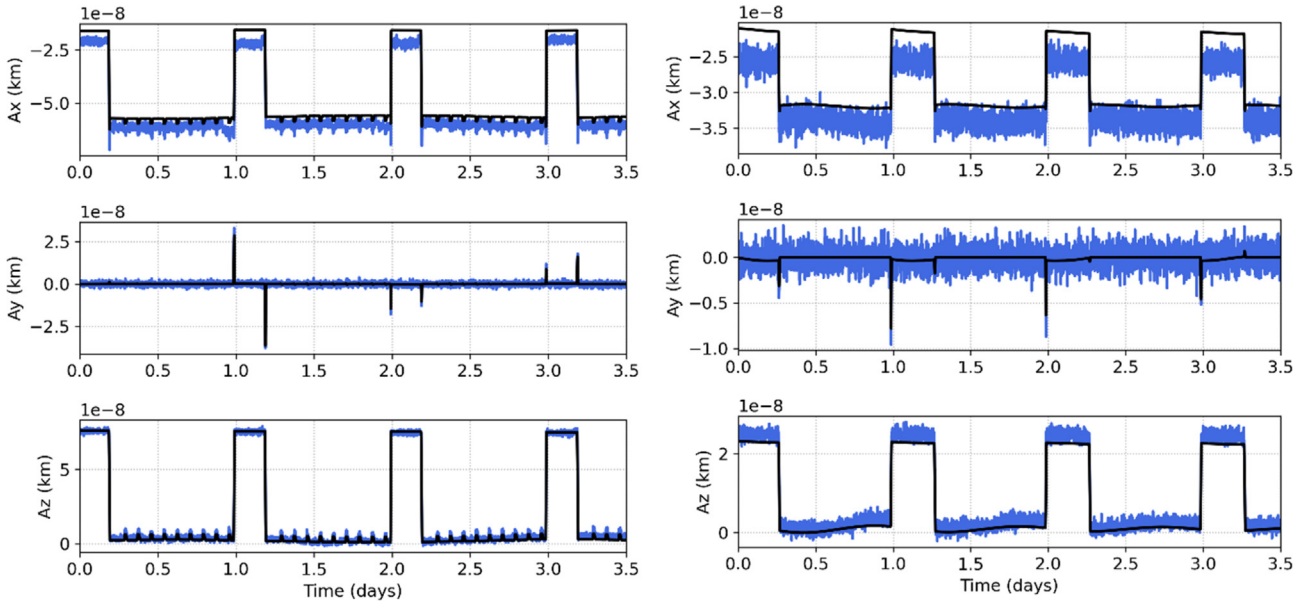

Fig. 6. XYZ components of the observations simulated along the NAIF–true trajectory (blue) and computed (black) measurements simulated along the reference trajectory, for a $1x10^{-9}$ m/s^2 sensitivity, for Orbit A (left) and Orbit B (right) expressed in the spacecraft frame.

which appears as discrepancy in the X and Z directions, depending on whether the spacecraft is in the Earth or Sun–pointing orientation. In addition, the thermal radiation pressure effect is greatest in the X spacecraft direction. Thus, its exclusion from the filter propagation leads to a discrepancy between the observed and computed measurements in that direction.

Fig. 7 shows the difference between the observed measurements, simulated along the NAIF–true trajectory, and the computed measurements, simulated along the filter reference trajectory, for both orbits. The accelerometer sensitivity of $1x10^{-9}$ m/s^2 is sufficient to observe the overall features of the non–gravitational force modeling error, which are on the order of $0.5–1.5x10^{-8}$ m/s^2 for Orbit A and $2.5–5x10^{-9}$ m/s^2 for Orbit B. However, some of the smaller features are obscured by the measurement noise.

4.3. Filter and accelerometer measurement processing set-up

The filter state (X) includes the XYZ position and velocity deviations from the reference trajectory for the OREx spacecraft in the EME2000 frame. In addition to the

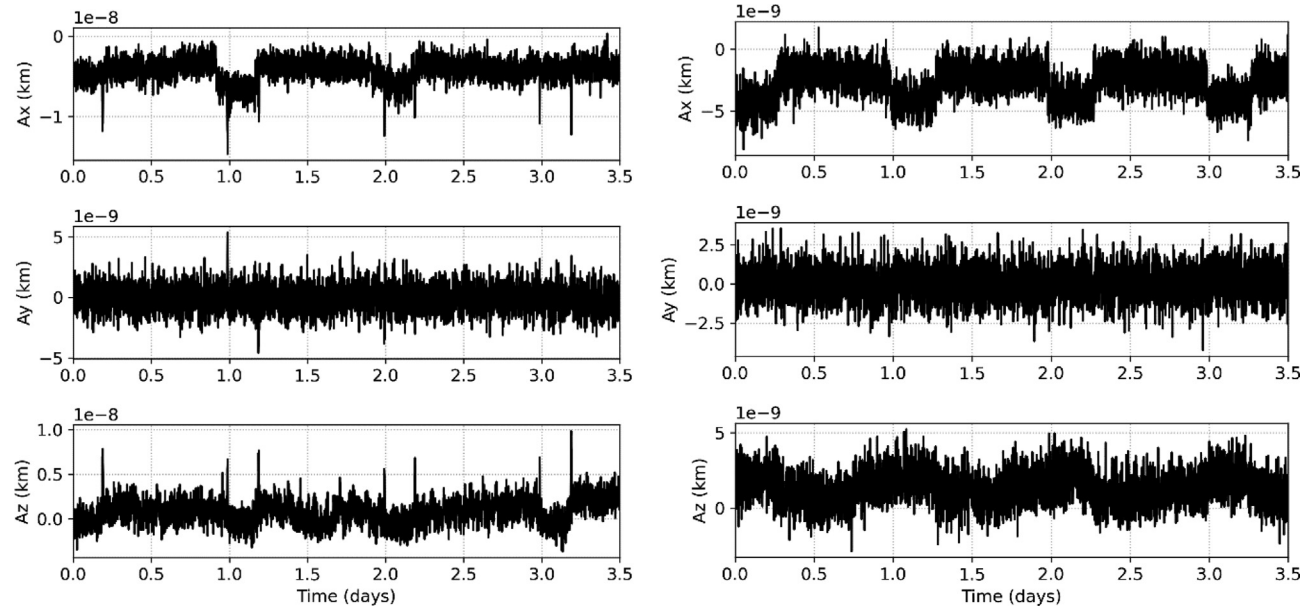

Fig. 7. XYZ components of the observations simulated along the NAIF–true trajectory minus computed measurements simulated along the filter reference trajectory, for a $1x10^{-9}$ m/s^2 sensitivity, for Orbit A (left) and Orbit B (right) expressed in the spacecraft frame.

position and velocity the filter includes stochastic acceleration, estimated to account for the unmodeled accelerations. The stochastic acceleration for each component is modeled as a mean–zero white noise process, in the spacecraft frame. The stochastic acceleration (a_i) is incorporated into the filter as shown in Eq. (4) (shown for the X axis in the spacecraft frame),

$$\begin{bmatrix} x_{x,i+1} \\ [\dot{x}_{x,i+1}] \\ a_{x,i+1} \end{bmatrix} = \begin{bmatrix} 1 & \Delta t & \Delta t^2/2 \\ 0 & 1 & \Delta t \\ 0 & 0 & 0 \end{bmatrix} \begin{bmatrix} x_{x,i} \\ [\dot{x}_{x,i}] \\ a_{x,i} \end{bmatrix} + \begin{bmatrix} 0 \\ 0 \\ 1 \end{bmatrix} w_{x,i} \quad (4)$$

where Δt is the filter step-size, $\dot{x}_i$ is the velocity, x_i is the position, and $w_{x,i}$ is the white noise process (Ely, Heyne, & Riedel, 2012). This allows the filter to absorb unmodeled accelerations into the stochastic XYZ informed by the noise sigma of $w_{x,i}$. The noise strength is determined by the size of the unmodeled gravitational and non–gravitational force acceleration errors induced by the mismodeling in the reference trajectory.

The accelerometer measurements relate to the stochastic acceleration via the measurement equation (shown for the X–axis in the spacecraft frame),

$$\Delta V_{x,i} = a_{x,i}\Delta t + v_{x,i} \quad (5)$$

and subsequent measurement partial matrix,

$$\frac{\partial \Delta V_{x,i}}{\partial X_i} = [0_{1x3} \quad 0_{1x3} \quad \Delta t \quad 0 \quad 0] \quad (6)$$

The accelerometer measurements are processed directly in the filter as done by Ely, Heyne, and Riedel (2012). This is in contrast to a dead reckoning approach commonly used in inertial navigation systems, where accelerometer measurements are used to propagate the trajectory, as presented in Jekeli (2005).

Table 6
Orbit A and B RMS.

Orbit	Accelerometer Sensitivity per Shot (m/s^2)	RMS (m)					
		Full DSN			Reduced DSN		
		R	T	N	R	T	N
A	None	5.0	11.8	2.4	5.1	19.6	2.7
	1x10^{-8}	3.0	6.1	1.8	3.3	8.4	2.1
	1x10^{-9}	3.0	5.9	1.8	3.2	8.2	2.0
	1x10^{-10}	2.9	5.9	1.8	3.2	8.1	2.0
B	None	1.3	4.8	0.5	1.3	6.9	0.7
	1x10^{-8}	0.8	3.4	0.4	0.9	3.6	0.4
	1x10^{-9}	0.8	2.6	0.4	0.9	3.5	0.4
	1x10^{-10}	0.8	2.6	0.4	0.9	3.4	0.4

5. OREx simulation results

The filter was run for full and reduced DSN pass cases for Orbit A and B. The first scenario uses all the daily passes, representing the pass configuration available during the actual OREx mission (Antreasian, et al., 2016). The second scenario removes the third and fourth pass for Orbit A and B respectively. Ten unique profiles of initial condition and measurement error were constructed. These profiles were applied to each scenario for a DSN only case and for several accelerometer sensitivity configurations. Each of the ten run sets used the same initial condition error and DSN and accelerometer measurement sensitivity

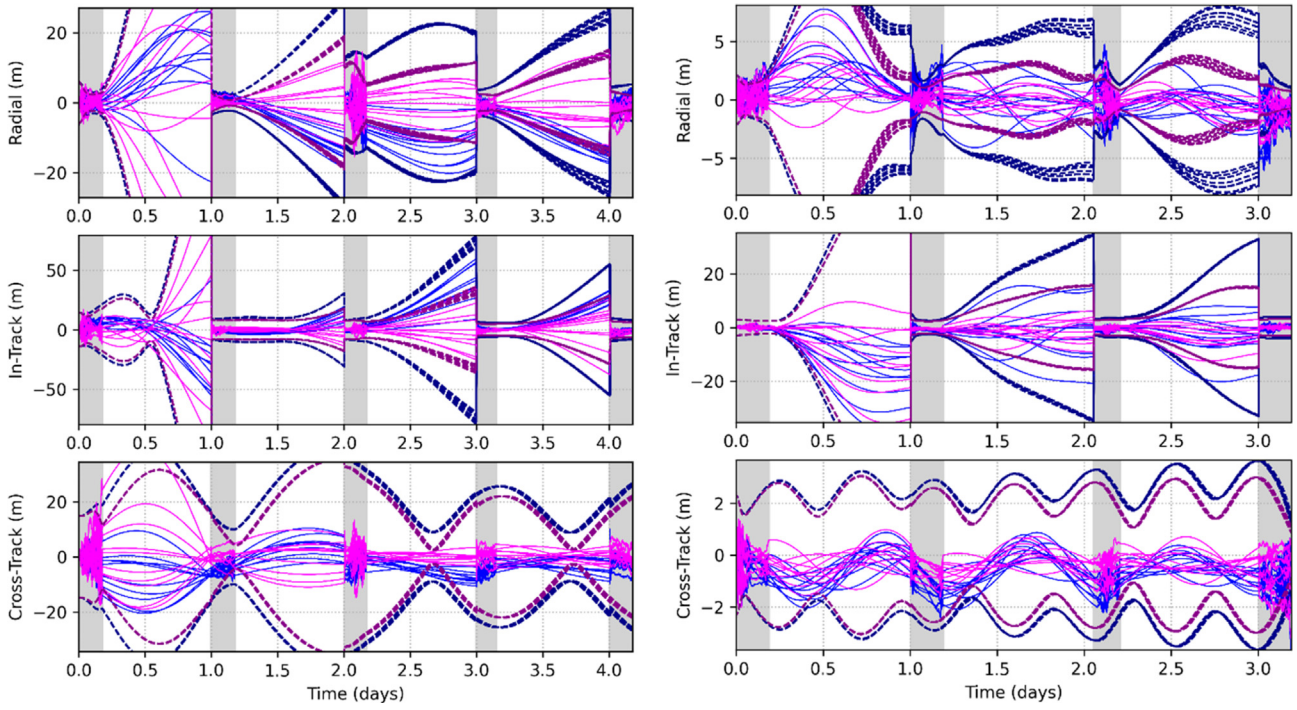

Fig. 8. Daily DSN passes – position errors and 1σ covariance bounds (dark/dashed) without (blue) and with (magenta) 1x10^{-9} m/s^2 sensitivity accelerometer measurements for Orbit A (left) and Orbit B (right) – RTN frame.

realizations. The average position RMS for each component for each of the ten runs are shown in Table 6, expressed in the RTN frame. The RMS is calculated from the start of the 3rd DSN pass for Orbit A and 2nd pass for Orbit B, to allow for filter convergence. Fig. 8 shows the position estimation error and 1σ bounds for the daily pass (passes shown in grey) configuration, for DSN measurements only (blue) and $1x10^{-9}$ m/s^2 accelerometer measurements (magenta) configurations.

The inclusion of accelerometer measurements improves the navigation performance for both orbit phases. Using accelerometers with sensitivity less than $1x10^{-9}$ m/s^2 results in only marginal improvement. Examining Fig. 6 and Fig. 7, the primary benefit of the accelerometers is from capturing the non–gravitational force profile features that are on the order of $1x10^{-9}$ m/s^2. During the real Orbit A mission phase, SRP scale factor and gravity parameters were estimated, allowing position resolution to 10-meter levels (Antreasian, et al., 2016; Williams, et al., 2018). SRP is the largest acceleration for Orbit A (aside from Gm), and an order of magnitude larger than SPH, so capturing the non–gravitational forces with the accelerometers allows for an improvement in estimation from tens of meters to less than 10 m. For Orbit B, the SRP surface forces and the uncertainty in the SPH gravitational forces are of very similar magnitude. The addition of the accelerometers for Orbit B improves the position resolution by a few meters. The reduction in error overall is less in the case of Orbit B than A, but there is a relative reduction, from the DSN only to the $1x10^{-9}$ m/s^2 sensitivity case, of 40 % in radial, 50 % in in–track and 20 % in cross–track errors, for both orbits.

Overall, we find that the navigation performance achieved in both orbit scenarios, with reduced DSN tracking and onboard accelerometers, is comparable to or better than the use of a full DSN daily tracking schedule with no accelerometers. Using the onboard accelerometers helps resolve the non–gravitational accelerations, subsequently improving the ability to determine the gravity field from the radiometric measurements. Furthermore, the use of SLI–based accelerometers could reduce the dependence on high accuracy non–gravitational force modeling and expanded filter state vectors to estimate systematic disturbances, allowing for the navigation filter state vector to includes only the vector components of position, velocity, and stochastic acceleration.

6. Conclusion

The advancement of compact precision accelerometers based on shaken lattice interferometry (SLI) provides an opportunity to consider future space exploration missions with greater autonomy and flexibility to observe and adapt to unexpected dynamical conditions. In this study, we analyzed of the use of precise SLI–based accelerometers for an OREx type mission, choosing this mission because of the unique challenges faced in navigating at very low altitudes above a very small body. These small orbits, only weakly held by Bennu's gravity, are substantially perturbed by solar radiation pressure – which is highly variable due to eclipse conditions and significant changes in spacecraft orientation. It is therefore an ideal case study to establish the levels of accelerometer performance useful for future space missions. For this scenario we found that a sensitivity of $1x10^{-9}$ m/s^2 is required to capture relevant surface accelerations and have a meaningful impact on navigation performance. Reduction in acceleration sensitivity below that level provides no appreciable navigation benefit without a corresponding improvement in knowledge of the gravitational field. In addition, the utilization of onboard accelerometers was shown to allow for a reduction of at least a day in required DSN tracking while maintaining similar navigation performance. This study used real reconstructed truth from the NAIF database to provide the most realistic simulation of dynamical errors possible, and JPL's MONTE software to provide a high–fidelity simulation comparison.

The analysis presented did not consider the potential for estimating Bennu's gravity field using a combination of DSN and SLI–based accelerometer measurements. This configuration would be similar to the high–fidelity Earth–gravity mapping performed by the GRACE and GOCE missions (Christophe B., 2013). Precise in-situ measurement of non-gravitational forces with SLI accelerometers would reduce the need to estimate parameters of complex models for SRP and thermal radiation and improve the observability of the central body gravitational constant (Gm) and higher order spherical harmonic components of the gravity field. Migliaccio et al. (2019) proposed the Mass Observation with Cold Atom Sensors in Space (MOCASS) mission, a GRACE/GOCE analog gravity mapping mission using onboard cold atom sensors, but to date it remains only a mission concept (Pivetta, Braitenberg, & Barbolla, 2021).

Funding

The work by M. Rybak and P. Axelrad is supported by the NSF QII–TAQS award number 1936303.

Declaration of Competing Interest

The authors declare that they have no known competing financial interests or personal relationships that could have appeared to influence the work reported in this paper.

Acknowledgements

The authors are grateful to Dr. Jason Leonard and Dr. Jeroen Geeraert from KinetX for providing data and guidance for the use of the OREx NAIF reconstructed trajectories. Additional thanks to Liang-Ying Chih and Professor Murray Holland for the helpful discussions on the operation of CAI/SLI–based accelerometers. The work

by M. Rybak and P. Axelrad is supported by the NSF QII–TAQS award number 1936303.

References

Abrykosov, P., Pail, R., Gruber, T., Zahzam, N., Bresson, A., Hardy, E., Christophe, B., Bidel, Y., Carraz, O., Siemes, C., 2019. Impact of a novel hybrid accelerometer on satellite gravimetry performance. Adv. Space Res. 63 (10), 3235–3248. https://doi.org/10.1016/j.asr.2019.01.034.

Albers, H. (2020). *Time-Averaged Optical Potentials for Creating and Shaping Bose-Einstein Condensates.* Hannover, Germany: Leibniz University Hannover, PhD Thesis. doi:10.15488/10073.

Antreasian, P. G., Moreau, M., Jackman, C., William, K., Page, B., & Leonard, J. M. (2016). OSIRIS-REx Orbit Determination Covariance Studies at Bennu. *34th Annual AAS Guidance and Control Conference.* Breckenridge, CO.

Barnouin, O. S., Daly, M. G., Palmer, E. E., Gaskell, R. W., Weirich, J. R., Johnson, C. L., Al Asad, M. M., Roberts, J. H., Perry, M. E., Susorney, H. C. M., Daly, R. T., Bierhaus, E. B., Seabrook, J. A., Espiritu, R. C., Nair, A. H., Nguyen, L., Neumann, G. A., Ernst, C. M., Boynton, W. V., Nolan, M. C., Adam, C. D., Moreau, M. C., Rizk, B., Drouet D'Aubigny, C. Y., Jawin, E. R., Walsh, K. J., Michel, P., Schwartz, S. R., Ballouz, R.-L., Mazarico, E. M., Scheeres, D. J., McMahon, J. W., Bottke, W. F., Sugita, S., Hirata, N., Hirata, N., Watanabe, S.-i., Burke, K. N., DellaGiustina, D. N., Bennett, C. A., Lauretta, D. S., & The OSIRIS-REx Team. (2019). Shape of (101955) Bennu indicative of a rubble pile with internal stiffness. *Nature Geoscience, 12*, 247-252. doi:https://doi.org/10.1038/s41561-019-0330-x.

Battelier, B., Barrett, B., Fouché, L., Chichet, L., Antoni-Micollier, L., Porte, H., Napolitano, F., Lautier, J., & Bouyer, P. (2016). Development of Compact Cold-Atom Sensors for Intertial Navigation. *Proceedings of SPIE, 9900*, pp. 990004-(1-17). Brussels, Belgium. doi:10.48550/arXiv.1605.02454.

Berry, K., Antresian, P., Moreau, M., Michael, C., May, A., & Brian, S. (2015). OSIRIS-REx Touch-And-Go (TAG) Navigation. *38th Annual AAS Guidance and Control Conference.* Breckenridge, Colorado.

Bhatia, R., Geller, D., 2020. Sensitivity analysis of precision inertial sensor-based navigation system (SAPIENS). J. Inst. Navig. 67 (4), 795–822. https://doi.org/10.1002/navi.397.

Canciani, A. J. (2012). *Integration of Cold Atom Interferometry INS with Other Sensors.* Wright-Patterson Air Force Base, Ohio: Department of the Air Force Air University: Air Force Institute of Technology, MS Thesis.

Canuel, B., Leduc, F., Holleville, D., Gauguet, A., Fils, J., Virdis, A., Clairon, A., Dimarcq, N., Borde, C.J., Landragin, A., 2006. Six-axis inertial sensor using cold-atom interferometry. Phys. Rev. Lett. 97 (1), 010402–010406. https://doi.org/10.1103/PhysRevLett.97.010402.

Carnal, O., Mlynek, J., 1991. Young's double-slit experiment with atoms: a simple atom interferometer. Phys. Rev. Lett. 66 (21), 2689–2694. https://doi.org/10.1103/PhysRevLett.66.2689.

Carraz, O., Siemes, C., Massotti, L., Haagmans, R., Silvestrin, P., 2014. A spaceborne gravity gradiometer concept based on cold atom interferometers for measuring earth's gravity field. Microgravity Sci. Technol. 26 (3), 139–145. https://doi.org/10.1007/s12217-014-9385-x.

Chiow, S.-W., Williams, J., Yu, N., 2015. Laser-ranging long-baseline differential atom interferometers for space. Phys. Rev. A, Atomic, Mol., Opt. Phys. 92 (6), 1–6. https://doi.org/10.48550/arXiv:1502.00047.

Christophe, B., 2013. GRACE & GOCE Experience. *Testing the Equivalence Principle: MICROSCOPE Colloquium II.* ONERA: The French Aerospace Lab, Palaiseau, France.

Christophe, B., Marque, J. P., & Foulon, B. (2010). In-Orbit Data Verification of the Accelerometers of the ESA GOCE Mission. *SF2A-2010: Proceedings of the Annual meeting of the French Society of Astronomy and Astrophysics*, (pp. 113-116). Marseille, France.

Christophe, B., Foulon, B., Liorzou, F., Lebat, V., Boulanger, D., Huynh, P. A., Zahzam, N., Bidel, Y., & Bresson, A. (2017). Status of Development of the Future Accelerometers for Next Generation Gravity Missions. *Proceedings of the IAG Scientific Assembly, International Symposium on Advancing Geodesy in a Changing World,*, (pp. 85-89). Kobe, Japan. doi:10.1007/1345_2018_42.

Clauser, J.F., 1988. Ultra-high sensitivity accelerometers and gyroscopes using neutral atom matter-wave interferometry. Physica B + C 151 (1), 262–272.

Conklin, J.W., 2015. Drift mode accelerometry for spaceborne gravity measurements. J. Geod. 89 (11), 1053–1070. https://doi.org/10.48550/arXiv.1402.6772.

Dutta, I., Savoie, D., Fang, B., Venon, B., Garrido Alzar, C.L., Geiger, R., Landragin, A., 2016. Continuous cold-atom inertial sensor with 1 nrad/sec rotation stability. Phys. Rev. Lett. 116 (18), 183003–183008. https://doi.org/10.1103/PhysRevLett.116.183003.

Ely, T.A., Heyne, M., Riedel, J.E., 2012. Altair navigation performance during translunar cruise, lunar orbit, descent, and landing. J. Spacecr. Rocket. 49 (2), 295–317. https://doi.org/10.2514/1.52233.

Fan, Y., Liang, L., Wang, C., Luo, Z., 2022. Attitude determination for GRACE-FO: reprocessing the level-1A SC and IMU data. Remote Sensing, Basel, Switzerland 14 (1), 126–150. https://doi.org/10.3390/rs14010126.

Flury, J., Bettadpur, S., Tapley, B.D., 2008. Precise accelerometry onboard the GRACE gravity field satellite mission. Adv. Space Res. 42 (8), 1414–1423. https://doi.org/10.1016/j.asr.2008.05.004.

French, A. S. (2020). *Precise Orbit Determination And Gravity Field Estimation During Small Body Mission.* Boulder, CO: University of Colorado, Boulder, PhD Thesis.

Geeraert, J. L., Leonard, J. M., Kenneally, P. W., Antreasian, P. G., Moreau, M., & Lauretta, D. S. (2020). OSIRIS-REx Navigation Small Force Models. *Advances in the Astronautical Sciences, AAS/AIAA Astrodynamics Specialist Conference, 171*, pp. 931-946. Portland, OR.

Getzandanner, K., Rowlands, D., Mazarico, E., Antreasian, P., Jackman, C., & Moreau, M. (2016). An Independent Orbit Determination Simulation for the OSIRIS-REx Asteroid Sample Return Mission. *39th Annual AAS Guidance & Control Conference.* Breckenridge, CO.

Hesar, S. G., Scheeres, D. J., & McMahon, J. W. (2016). Analysis of Solar Radiation Pressure Effects on the OSIRIS-REX Spacecraft in Orbit Around Bennu. *26th AAS/AIAA Space Flight Mechanics Meeting.* Napa, CA.

Hogan, J.M., Kasevich, M.A., 2016. Atom-interferometric gravitational-wave detection using heterodyne laser links. Phys. Rev. A 94 (3), 1–12. https://doi.org/10.48550/arXiv.1501.06797.

Jekeli, C., 2006. Precision free-inertial navigation with gravity compensation by an onboard gradiometer. J. Guid. Control Dynam. 29 (3), 704–714. https://doi.org/10.2514/1.15368.

Jekeli, C. (2005). Navigation Error Analysis of Atom Interferometer Inertial Sensor. *Navigation: Journal of the Institute of Navigation, 52* (1), 1-14. doi:10.1002/j.2161-4296.2005.tb01726.x.

Kang, Z., Tapely, B., Bettadpur, S., Ries, J., & Nagel, P. (2006). Precise orbit determination for GRACE using accelerometer data. *Advances in Space Research*, 2131-2136. doi:doi:10.1016/j.asr.2006.02.021.

Kasevich, M., 2007. Cold Atom Navigation Sensors. Stanford University, Standord, CA, Position Navigation and Timing Symposium Brief.

Kasevich, M., Chu, S., 1991. Atomic interferometry using stimulated Raman transitions. Phys. Rev. Lett. 67 (2), 181–184. https://doi.org/10.1103/PhysRevLett.67.181.

Kenneally, P. W. (2019). *Faster than Real-Time GPGPU Radiation Pressure.* Boulder, CO: University of Colorado, Boulder, PhD Thesis.

Klinger, B., Mayer-Gurr, T., 2016. The role of accelerometer data calibration within GRACE gravity field recovery: results from ITSG-Grace2016. Adv. Space Res. 58 (9), 1597–1609. https://doi.org/10.1016/j.asr.2016.08.007.

Lauretta, D. S., Balram-Knutson, S. S., Beshore, E., Boynton, W. V., Drouet d'Aubigny, C., DellaGiustina, D. N., Enos, H. L., Golish, D. R., Herfenrother, C. W., Howell, E. S., Bennett, C. A., Morton, E. T., Nolan, M. C., Rizk, B., Roper, H. L., Bartels, A. E., Bos, B. J.,

Dworkin, J. P., Highsmith, D. E., Lorenz, D. A., Lim, L. F., Mink, R., Moreau, M. C., Nuth, J, A., Reuter, D.C., Simon, A. A., Bierhaus, E. B., Bryan, B. H., Ballouz, R., Barnouin, O. S., Binzel, R. P., Bottke, W. F., Hamilton, V. E., Walsh, K. J., Chesley, S. R., Christensen, P. R., Clark, B. E., Connolly H. C., Crombie, M. K., Daly, M.G., Emery, J. P., McCoy, T. J., McMahon, J. W., Scheeres, D. J., Messenger, S., Nakamura-Messenger, K., Righter, K., & Sandford, S. A. (2017). OSIRIS-REx: Sample Return from Asteroid (101955) Bennu. *Space Science Review, 212*(1-2), 925-984. doi:10.1007/s11214-017-0405-1.

Lautier, J., Volodimer, L., Hardin, T., Merlet, S., Lours, M., Pereira Dos Santos, F., Landragin, A., 2014. Hybridizing matter-wave and classical accelerometers. Appl. Phys. Lett. 105 (14), 1–4. https://doi.org/10.48550/arXiv.1410.0050.

Leonard, J. M., Geeraert, J. L., Page, B. R., French, A. S., Antreasian, P. G., Adam, C. D., Wibben, D. R., Moreau, M. C., & Lauretta, D. S. (2019). OSIRIS-Rex Orbit Determination Perfomance During the Navigation Campaign. *AAS/AIAA Astrodynamics Specialist Conference.* Portland, ME.

Leveque, T., Fallet, C., Mandea, M., Biancale, R., Lemoine, J.M., Tardivel, S., Delavault, S., Piquereau, A., Borgogne, S., Pereira Dos Santos, F., Battelier, B., Couyer, P.h., 2021. Gravity field mapping using laser coupled quantum accelerometers in space. J. Geod. 95 (1), 1–32. https://doi.org/10.48550/arXiv.2011.03382.

Meunier, M., Dutta, I., Geiger, R., Guerlin, C., Garrido Alzar, C. L., & Landragin, A. (2014). Stability Enhancement by Joint Phase Measurements in a Single Cold Atomic Fountain. *Physical Review. A, Atomic, Molecular, and Optical Physics, 90*(6), 063633-(1-5). doi:10.1103/PhysRevA.90.063633.

Migliaccio, F., Reguzzoni, M., Batsukh, K., Tino, G.M., Rosi, G., Sorretino, F., Braitenberg, C., Pivetta, T., Francesca Barbolla, D., Zoffoli, S., 2019. MOCASS: a satellite mission concept using cold atom interferometry for measuring the earth gravity field. Surv. Geophys. 40 (5), 1029–1053. https://doi.org/10.1007/s10712-019-09566-4.

NASA: Jet Propulsion Laboratory. (2021, March 26). *Mission Analysis, Operations, and Navigation Toolkit (MONTE) Documentation.* (Caltech/Jet Propulsion Laboratory) Retrieved April 7, 2021, from https://monte.jpl.nasa.gov/doc/current/index.html.

Nyman, R.A., Varoquaux, G., Lienhart, F., Chambon, D., Boussen, S., Clement, J.F., Muller, T., Santarelli, G., Pereira Dos Santos, F., Clairon, A., Bresson, A., Ladragin, A., Bouyer, P., 2006. I.C.E.: a transportable atomic inertial sensor for test in microgravity. Appl. Phys. B Lasers Opt. 84 (4), 673–681. https://doi.org/10.1007/s00340-006-2395-7.

OSIRIS-REx Asteroid Sample Return Mission. (2022). (Arizona Board of Regents) Retrieved Feb 07, 2022, from https://www.asteroidmission.org/objectives/objectives-3/.

Peidou, A., Pagiatakis, S., 2019. Gravity gradiometry with GRACE space missions: new opportunities for the geosciences. J. Geophys. Res. Solid Earth 124 (8), 9130–9147. https://doi.org/10.1029/2018JB016382.

Pivetta, T., Braitenberg, C., Barbolla, D.F., 2021. Geophysical challenges for future satellite gravity missions: assessing the impact of MOCASS mission. Pure Appl. Geophys. 178 (6), 2223–2240. https://doi.org/10.1007/s00024-021-02774-3.

Reguzzoni, M., Migliaccio, F., Batsukh, K., 2021. Gravity field recovery and error analysis for the MOCASS mission proposal based on cold atom interferometery. Pure Appl. Geophys. 178 (6), 2201–2222. https://doi.org/10.1007/s00024-021-02756-5.

Roy, R., Green, A., Bowler, R., & Gupta, S. (2016). Rapid Cooling to Quantum Degeneracy in Dynamically Shaped Atom Traps. *Physical Review A, 93*(4), 043403-(1-7). doi:10.48550/arXiv.1601.05103.

Rozitis, B., Ryan, A. J., Emery, J. P., Christensen, P. R., Hamilton, V. E., Simon, A. A., Reuter, D. C., Al Asad, M., Ballouz, R. L., Bandfield, J. L., Barnouin, O. S., Bennett, C.A., Bernacki, M., Burke, K. N., Cambioni, S., Clark, B. E., Daly, M. G., Delbo, M., DellaGiustina, D. N., Elder, C. M., Hanna, R. D., Haberle C. W., Howell, E. S., Golish, D. R., Jawin, E. R., Kaplan, H. H., Lim, L. F., Molaro, J. L., Pino Munoz, D., Nolan, M. C., Rizk, B., Siegler, M. A., Sursorney, H. C. M., Walsh, K. J., & Lauretta, D. S. (2020). Asteroid (101955) Bennu's Weak Boulders and Thermally Anomalous Equator. *Science Advances, 6*(41), eabc3699-(1-18). doi:10.1126/sciadv.abc3699.

Rummel, R., Yi, W., Stummer, C., 2011. GOCE gravitational gradiometry. J. Geod. 85 (11), 777–790. https://doi.org/10.1007/s00190-011-0500-0.

Semenov, B. (2014, June 6). *OSIRIS-REx (ORX) Frames Kernel.* (Navigation and Ancillary Information Facility) Retrieved June 18, 2021, from https://naif.jpl.nasa.gov/pub/naif/ORX/kernels/fk/orx_v03.tf.

Theurkauf, A. (2020). *Control of an Optical Lattice for Atom-Based Inertial Sensing.* Boulder, CO: University Of Colorado, Boulder, MS Thesis.

Titterton, D.H., Weston, J.L., 2004. Chapter 2: Fundamental Principles and Historical Developments of Inertial Navigation. In: Strapdown Inertial Navigation Technology, 2nd Edition. Institution of Electrical Engineers, Reston, VA, pp. 7–16. https://doi.org/10.1049/PBRA017E.

Touboul, P., 2003. Microscope instrument develoment, lessons for GOCE. Space Sci. Rev. 108 (1), 393–408. https://doi.org/10.1023/A:1026152114467.

Touboul, P., Foulon, B., Rodrigues, M., & Marque, J. P. (2004). In orbit nano-g measurements, lessons for future space missions. *Aerospace Science and Technology, 8*, 431-441. doi:doi:10.1016/j.ast.2004.01.006.

Touboul, P., Willemenot, E., Foulon, B., Josselin, V., 1999. Accelerometers for CHAMP, GRACE and GOCE space missions: synergy and evolution. Boll. Geofis. Teor. Appl. 40 (3–4), 321–327.

Trimeche, A., Battelier, B., Becker, D., Bertoldi, A., Bouyer, P., Braxmaier, C., Charron, E., Corgier, R., Cornelius, M., Douch, K., Gaaloul, N., Herrmann, S., Muller, J., Rasel, E., Schubert, C., Wu, H., & Pereira Dos Santos, F. (2019). Concept Study and Preliminary Design of a Cold Atom Interferometer for Space Gravity Graiometry. *Classical and Quantum Gravity, 36*(21), 215004-(1-40). doi:10.48550/arXiv.1903.09828.

Visser, P.A., 2008. GOCE gradiometer: estimation of biases and scale factors of all six individual accelerometers by precise orbit determination. J. Geod. 83 (1), 69–85. https://doi.org/10.1007/s00190-008-0235-8.

Weidner, C. A., & Anderson, D. Z. (2018). Experimental Demonstration of Shaken-Lattice Interferometry. *Physical Review Letters, 120*(26), 263201-(1-5). doi:10.1103/PhysRevLett.120.263201.

Weidner, C. A., & Anderson, D. Z. (2018). Simplified Landscapes for Optimization of Shaken Lattice Interferometry. *New Journal of Physics, 20*(7), 75007-(1-13). doi:10.48550/arXiv.1803.01235.

Weidner, C. A., Yu, H., Kosloff, R., & Anderson, D. Z. (2017). Atom Interferometry Using a Shaken Optical Lattice. *Physical Review A, 95*(4), 043624-(1-10). doi:10.1103/PhysRevA.95.043624.

Weidner, C. A. (2019). *Shaken Lattice Interferomerty.* Boulder, CO: University of Colorado, Boulder, PhD Thesis.

Williams, B., Antreasian, P., Carranza, R., Jackman, C., Leonard, J., Nelson, D., Page, B., Stanbridge, D., Wibben, D., Williams, K., Moreau, M., Berry, K., Getzandanner, K., Liounis, A., Mashiku, A., Highsmith, D., Sutter, B., Lauretta, D.S., 2018. OSIRIS-REx flight dynamics and navigation design. Space Sci. Rev. 214 (4), 1–43. https://doi.org/10.1007/s11214-018-0501-x.

Xu, V., Jaffe, M., Panda, C.D., Kristensen, S.L., Clark, L.W., Muller, H., 2019. Probing gravity by holding atoms for 20 seconds. Science (Am. Assoc. Adv. Sci.) 366 (6466), 745–749. https://doi.org/10.1126/science.aay6428.